Author Manuscript

Author Manuscript

Author Manuscript

Author Manuscript

HHS Public Access

Author manuscript

IEEE Trans Ultrason Ferroelectr Freq Control. Author manuscript; available in PMC 2018 February 28.

Published in final edited form as:

IEEE Trans Ultrason Ferroelectr Freq Control. 2017 June ; 64(6): 910–921. doi:10.1109/TUFFC.2017.2683559.

Blocked Elements in 1-D and 2-D Arrays—Part I: Detection and Basic Compensation on Simulated and *In Vivo* Targets

Marko Jakovljevic,

Department of Biomedical Engineering, Duke University, Durham, NC 27708 USA. He is now with the Department of Radiology, Stanford School of Medicine, Stanford, CA 94305 USA

Gianmarco F. Pinton,

Joint Department of Biomedical Engineering, University of North Carolina at Chapel Hill and North Carolina State University, Chapel Hill, NC 27599 USA

Jeremy J. Dahl [Member, IEEE], and

Department of Radiology, School of Medicine, Stanford University, Stanford, CA 94305 USA

Gregg E. Trahey [Member, IEEE]

Department of Biomedical Engineering, Duke University, Durham, NC 27708 USA, and also with the Department of Radiology, Duke University Medical Center, Durham, NC 27708 USA

Abstract

During a transcostal ultrasound scan, ribs and other highly attenuating and/or reflective tissue structures can block parts of the array. Blocked elements tend to limit the acoustic window and impede visualization of structures of interest. Here, we demonstrate a method to detect blocked elements and we measure the loss of image quality they introduce in simulation and *in vivo*. We utilize a fullwave simulation tool and a clinical ultrasound scanner to obtain element signals from fully sampled matrix arrays during simulated and *in vivo* transcostal liver scans, respectively. The elements that were blocked by a rib showed lower average signal amplitude and lower average nearest-neighbor cross correlation than the elements in the remainder of the 2-D aperture. The growing receive-aperture B-mode images created from the element data indicate that the signals on blocked elements are dominated by noise and that turning them OFF has a potential to improve visibility of liver vasculature. Adding blocked elements to the growing receive apertures for five *in vivo* transcostal acquisitions resulted in average decrease in vessel contrast and contrast to noise ratio of 19% and 10%, respectively.

Index Terms

Blocked elements; 2-D arrays; ribs; transthoracic imaging; growing aperture; cross-correlation; full-wave simulation

Correspondence to: Marko Jakovljevic.

Author Manuscript Author Manuscript Author Manuscript Author Manuscript

I. Introduction

When imaging with ultrasound through the chest wall, it is not uncommon for parts of the array to be positioned against the ribs, preventing them from effectively transmitting and/or receiving acoustic pulses [1]. Other structures, such as scar tissue or air in the lungs, can also introduce a high acoustic impedance mismatch and block array elements, or parts of them, during an ultrasound scan [2], [3]. Blocked elements tend to significantly degrade overall image quality, limit the acoustic window, and impede visualization of the structures of interest [4]. With the development of large-aperture, high-element-count, 2-D arrays and their potential use in transthoracic imaging, detecting and compensating for the blocked elements are becoming increasingly important. In this paper, we focus on ways to detect blocked elements and to measure their impact on visibility of anechoic and hypoechoic targets *in vivo*.

The system architecture of most clinical ultrasound scanners makes it difficult to assess the problem of blocked elements *in vivo*. Typically, the raw echoes from individual elements can be collected from a clinical system only through custom pulse sequencing, which is difficult to realize in real time due to limits on the internal memory size and data-transfer rates, and lack of access to proprietary information. In addition, in most high-element count 2-D arrays, signals from the individual elements are partially beamformed in the handle of the transducer [5] and are not accessible even through custom sequencing; this prevents complete and precise characterization of blocked parts of the array. To the best of our knowledge, there have been no *in vivo* attempts to characterize signals on the blocked elements and to measure image-degradation they introduce. Li *et al.* [4] and O'Donnell and Engeler [6] suggested estimation of the signal amplitude and standard deviation across the aperture to identify blocked elements as statistical outliers, but did not demonstrate results that would verify the proposed method.

Several groups [7]–[9] have developed methods to detect acoustic blockage using beamformed data. In [7], the edges of blocked parts of the field-of-view (FOV) are detected based on low coherence between beamsummed data from different subapertures. In [8], the lateral power spectrum at the focus is used to infer shape of the active aperture and the locations of acoustic obstacles. The methods in [7] and [8] are designed to provide guidance on probe positioning in order to increase the acoustic window. Ballard *et al.* [9] used echogenecity (integrated backscatter) to determine locations of ribs prior to applying adaptive compensation on a dual-mode (imaging plus therapy) array.

There have been several *ex vivo* studies aimed at understanding the mechanisms and extent of image degradation in transthoracic ultrasound. Notably, Hinkelman *et al.* [1] measured arrival-time and energy-level fluctuations across a mechanically scanned 2-D aperture for ultrasonic wavefronts that propagated through the extracted samples of human chest wall. The average rms values were 21.3 ns and 1.57 dB for the arrival-time and energy-level fluctuations, respectively. The receive 2-D apertures were windowed to minimize parts blocked by bone and to isolate distortions introduced by soft-tissue inhomogeneities; the above-reported results are thus clinically relevant only for intercostal imaging with small arrays.

Author Manuscript Author Manuscript Author Manuscript Author Manuscript

As a part of their transcostal, high-intensity, focused ultrasound (HIFU) feasibility study, Aubry *et al.* [10] measured distortions of the ultrasound beam transmitted through the ribs. In simulation and *ex vivo* experiments, they found that waves that propagated through bone had a pressure amplitude about six times lower than waves that propagated through soft tissue (in between the ribs). Compared with the control transmit beampattern measured in the absence of acoustic obstacles, the beampatterns associated with transrib imaging experienced a mean spreading in the main lobe half width of 1.25 mm and an increase in the sidelobe levels of up to 20 dB. However, the transducer used in the *ex vivo* study was designed for HIFU experiments (transmitting at 1 MHz with 200 elements, 8 mm in diameter each), so the extent of beam distortion in the diagnostic imaging domain remains unknown.

Simulation studies in [11] and [12] offer a more systematic analysis of intensity distributions at the focal plane of an HIFU transducer during transrib therapy. In particular, both studies assessed the appearance of secondary foci due to the periodic structure of the ribs, the phenomenon known as focus splitting. Khokhlova *et al.* [11] simulated propagation from a phased array containing 254 randomly distributed elements (7 mm in diameter each), and predicted that ribs can cause the appearance of anywhere between one and five focal maxima, depending on the ratio of sizes of intercostal spaces and ribs. The diameter of each focus is similar to the diameter of the focal spot in the absence of ribs. In addition, the absolute intensities in the focal plane are a function of the position of ribs relative to the transducer surface; the maximum focus amplitude is achieved when the beam area covered by ribs is minimal. These conclusions were reached using diffraction theory and pursuing both analytic and numerical approaches. In all cases, a strong agreement was achieved between these solutions and intensity measurements from an *ex vivo* setup.

Gélat *et al.* [12] also simulated the acoustic field due to a multielement HIFU array delivering therapy transcostally and intercostally. They used a boundary-element approach in combination with phase conjunction. The ribs were assumed to be perfect reflectors and the model did not account for nonlinear wave propagation, which is in odds with an HIFU therapy simulation in [11], where ribs were assumed to be perfect absorbers. Nevertheless, for a densely spaced rib configuration, the locations of the secondary foci compare well between the two studies. The studies in [10]–[12] were all aimed at ultrasound therapy, and did not address the effect of beam degradation (due to blocked elements) on visibility of distributed and anechoic targets.

In this paper, we detect blocked elements in fully sampled 2-D apertures, and turn them OFF to compensate for the loss of target visualization in simulated and *in vivo* transcostal liver scans. In particular, for the first time, a full-wave simulation tool and a commercial 3-D ultrasound system are utilized to demonstrate a method for detecting blocked elements based on the amplitude and cross correlation of their signals. From the simulated and *in vivo* data, we also reconstruct B-mode images of liver vasculature using receive apertures with different numbers of blocked elements. We expect that turning OFF blocked elements will reduce the amount of acoustic noise in the image and will improve vessel contrast and contrast to noise ratio (CNR). In the companion paper, we apply adaptive blocked-element

Author Manuscript Author Manuscript Author Manuscript Author Manuscript

compensation schemes to large synthetic aperture data sets collected *ex vivo*, and we measure the resulting recovery of focus quality and the reduction of clutter levels.

II. Methods

A. Full-Wave Simulations

We simulated the received radio frequency signals from the individual elements from a fully sampled 2-D array while imaging the liver intercostally. We first created a 3-D acoustic map of parts of thorax and abdomen that would be captured in an intercostal liver scan, and then used full-wave code developed by Pinton *et al.* [13] to model wave propagation through the medium, including the effects of nonlinearity, attenuation, and multiple scattering (reverberation).

The 3-D acoustic map of tissue was built using the National Library of Medicine's Visible Human data set, which provides high resolution registered optical, MRI, and CT scans of entire male and female bodies. Following the procedure outlined in [14], each structure in the region of interest was declared as one of the six tissue types (homogeneous, fat, muscle, connective, liver, or bone tissue) and assigned appropriate values for its acoustic properties (speed of sound, density, nonlinearity, and attenuation). Acoustic properties of each tissue type were determined from the data compiled by Goss *et al.* [15], [16] and are listed in Table I. While the reported speed of sound in bone is as high as 3000 m/s, a significantly lower value (800 m/s) was used in the simulation in order to reduce the temporal sampling frequency needed to capture wave propagation (through the bone). Because this was a 3-D simulation with a spatial grid of over 400 million points, it was important to keep the number of time steps, and also the computation time and amount of data, at reasonable levels. The bone density was set so that the acoustic impedance mismatch between bone and soft tissue remained similar as in real tissue. This ensured that the amount of energy reflected from the soft-tissue/bone interfaces, and therefore, the attenuation of signals received by the blocked elements was modeled correctly.

In order to simulate speckle generating targets, small local variations in speed of sound (average variation of 5% from the surrounding tissue) were introduced throughout the modeled medium. The resulting point scatterers had a 40 um diameter and were randomly distributed with average density of 12 scatterers per 3-D resolution volume.

To assess quality of a simulated transcostal liver scan, a spherical anechoic lesion was inserted in the liver tissue model. The lesion was created at 6-cm depth by eliminating all point scatterers within a 3.5-mm radius. In addition, a set of modified acoustic maps was created for a control case by replacing ribs with the surrounding connective tissue; the resulting maps were otherwise the same as their transcostal counterparts. To illustrate the geometry of the imaged medium, the orthogonal slices of the (3-D) speed-of-sound maps are shown in Fig. 1 for both transcostal and control cases.

Having specified the acoustic properties of the tissue, wave propagation was simulated for transcostal and control scans. In both cases, in order to reconstruct complete B-mode images, five transmit events were simulated across the medium in the direction along the

Author Manuscript Author Manuscript Author Manuscript Author Manuscript

ribs (i.e., lateral dimension), similar to a diagnostic scanner operating in a linear imaging mode. The simulation code was run for each transmit event to numerically solve the full-wave equation (via FDTD method) giving the full pressure field at all times. The grid spacing for the simulation was set at 15 points per wavelength (matched to 2.5 MHz), and the pressure field was computed at each point of the grid over 9000 time steps with a sampling period of 0.0267 us. Initial conditions for solving the equation were set by prescribing the transmit waveforms at the location of the 2-D aperture. Individual channel signals were obtained by sampling the pressure field at the face of the transducer and convolving it with the axial transducer impulse response. Specifically, the center frequency of transmitted waves was set at 2.5 MHz and the transducer impulse response was set to yield a fractional bandwidth of 0.5. The 2-D aperture extended 1.9 cm in lateral and 1.4 cm in elevation dimension, and was positioned so that roughly one half of it was blocked by ribs during the transcostal scan. Specifications of the modeled transducer are listed in Table II. The individual channel signals from each transmit event were used to beamform 50 receive lines to ensure sufficient sampling in the lateral dimension.

B. In Vivo Single-Channel Acquisition

To acquire element data *in vivo*, we developed custom acquisition sequences on a modified Siemens Acuson SC2000 scanner and 4z1c matrix array (Siemens Medical Solutions USA, Inc., Mountain View, CA). This high-element-count 2-D array has both a lateral pitch and an elevational pitch of 0.4 mm. Array elements are grouped in square subapertures that are beamformed in the handle of the transducer to supply 192 system channels. Throughout these papers, data from an individual channel, therefore, refer to the beamformed data within a square subaperture.

The complex data of the individual channels were collected using a full-synthetic receive sequence, as implemented in [17]. In this method, the full aperture was used to transmit focused waves while parallel receive beamforming was used to collect signals on 30 channels per transmit event. Six transmits were fired per image line to collect data for 180 channels at the volume rate of two volumes per second. The complex data collected for each channel was sampled at a rate of 2.5 MHz, which was sufficient to obtain high-resolution ultrasound images.

The individual-channel data needed to reconstruct complete B-mode volumes were acquired on the liver vasculature of five human volunteers, ages 29 to 59. Written consent was obtained from all participants, and the study protocol was approved by the Duke University Medical Center Institutional Review Board. The data were acquired using a transmit frequency of 2.5 MHz and over the FOV that spanned 38° in lateral and 19.2° in elevation. Livers were first imaged intercostally, so that parts of the 2-D aperture were blocked by the ribs. To obtain control data (with all the transducer elements free to transmit and receive pulses), the same vasculature was also imaged subcostally, away from the ribs. In both cases, the probe was angled so that the vasculature of interest was in the middle of the FOV. To minimize motion artifacts, the patients were asked to hold their breath and to remain still for the duration of each half-a-second acquisition.

Author Manuscript Author Manuscript Author Manuscript Author Manuscript

C. Detection of Blocked Elements and Basic Compensation

For simulated and *in vivo* data sets, the magnitude and the nearest-neighbors normalized cross correlation of the individual element signals were computed to detect blocked elements. Kernel of 1.2 mm (two wavelengths) was used to calculate cross-correlation values. The two quantities were averaged axially, over a 4-cm range centered around the transmit focus to reduce clutter-induced variance and to improve detection of blocked elements in the receive 2-D aperture. Elements were classified as blocked if their depth-averaged amplitude was −8 dB or lower (compared with the maximum amplitude on the 2-D aperture), and if their nearest-neighbor normalized cross correlation was less than 0.5. The element signals with low amplitude and low nearest-neighbor normalized cross correlation are likely to be overwhelmed by noise, which can result in a loss of image quality and an inadequate visualization of the target.[1] The specific cutoff values of amplitude and cross correlation were determined empirically by those levels that defined a clear boundary between the regions of blocked and nonblocked elements. For the simulated transcostal acquisition, these regions were also compared with the anticipated locations of blocked elements based on the position of the rib in the acoustic maps.

In order to assess the impact of blocked elements on image quality and the effectiveness of basic blocked-element compensation, a series of simulated and *in vivo* B-mode images was created from the growing receive apertures. For each *in vivo* transcostal acquisition, the direction of aperture growth was chosen to provide a clear transition from the nonblocked to the blocked part of the aperture. For the simulated transcostal scan, the receive aperture was grown in the opposite direction to include the signals from the blocked elements first, because the image quality from the corresponding control experiment was more sensitive to the change in aperture size at small apertures. The direction of aperture growth was restricted to a single dimension (lateral or elevation) to mimic behavior of a 1-D array with partially blocked elements. This procedure amounted to summing the 2-D aperture data coherently along one dimension of the array, and then growing the resulting synthetic-receive, 1-D aperture in a manner as described by Bottenus *et al.* [18]. For the abdominal (and simulated control) data sets, the receive apertures were grown in the same direction as for the corresponding transcostal acquisitions.

The orientation and position of the reconstructed B-mode slices were the same for a given acquisition and were chosen to optimally capture hypoechoic structures of interest (lesions and liver vasculature). To compare image quality across the slices, the contrast and the CNR of these structures were calculated for each slice, according to the following equations:

$$\text{Contrast} = -20\log_{10}\left(\frac{S_i}{S_o}\right) \quad (1)$$

[1]This point is demonstrated in the left B-mode image in Fig. 6, which was created using only the signals from the blocked elements in the simulated transcostal scan. The image is saturated with noise and the anechoic lesion at 6-cm depth cannot be observed.

Author Manuscript Author Manuscript Author Manuscript Author Manuscript

$$\mathrm{CNR}=\frac{S_i-S_o}{\sqrt{\sigma_i^2+\sigma_o^2}}. \quad (2)$$

In (1) and (2), S_i and S_o are the mean signal magnitudes of the regions inside and outside of a hypoechoic structure, respectively, and σ_i^2 and σ_o^2 are the corresponding signal variances.

III. Results

A. Individual Element Signals

The average amplitude and the average nearest-neighbor normalized cross correlation of the simulated element signals are shown in Fig. 2. The receive-element signals are characterized for the middle transmit (Tx) beam of the simulated transcostal scan, and for the matching control simulation, where the ribs are substituted with connective tissue properties. The amplitude and the nearest-neighbor cross correlation are averaged over 4 cm of depth around the transmit focus, where the cross-correlation values are expected to follow the Van-Cittert–Zernike theorem [19]. For speckle signals corrupted by clutter, a large averaging range is necessary to reduce noise in the estimates of amplitude and the nearest-neighbor cross correlation. The two quantities are displayed across the receive (Rx) 2-D aperture using a linear grayscale map and the dynamic range of 0–1. For the control simulation [Fig. 2(a)], both quantities are relatively uniform across the array. For the transcostal simulation [Fig. 2(b)], the top four rows of elements, which are positioned over the rib in Fig. 1, display lower amplitude and cross-correlation values than the rest of the aperture. While there is an agreement between the amplitude and cross-correlation images for both simulations, the cross-correlation image created from the transcostal scan displays sharper boundaries of the blocked region (of the aperture) than its corresponding amplitude image.

Examples of amplitude and cross correlation of the individual-element signals acquired from the *in vivo* liver are presented in Figs. 3 and 4. The images are created from a transcostal and abdominal data set, both acquired from the liver of a 59-year-old male. Fig. 3 displays the depth-averaged amplitude and cross correlation over the extent of 2-D apertures for both acquisitions, in a similar manner as Fig. 2. For the abdominal acquisition [Fig. 3(a)], the two quantities exhibit high uniformity over the entire surface of the array. For the transcostal acquisition [Fig. 3(b)], a region of dark pixels located in the bottom-right corner of both images clearly shows the extent of the blocked part of the aperture. Due to angled orientation of the rib with respect to edges of the array during the acquisition, the shape of the blocked region can be fully inferred only using a matrix array. Signals received on this part of the array have 8.4-dB lower average amplitude than the signals received on the remainder of elements.

In Fig. 4, the average element amplitude and the average nearest-neighbor cross correlation are shown as functions of the transmit beam direction (in the lateral plane) for a single row of elements on the aperture. For the abdominal acquisition [Fig. 4(a)], the images are uniform and display high values (close to 1), which indicates that no obstacles are

Author Manuscript Author Manuscript Author Manuscript Author Manuscript

encountered in the acoustic path as the transmit beam is swept across the FOV. In the images reconstructed from the transcostal acquisition [Fig. 4(b)], a diagonal shape of the region of low values implies that the number blocked elements in the row of interest decreases as the Tx beam is steered away from the ribs.

B. Growing Aperture B-Mode Images

Visibility of anechoic and hypoechoic targets in the presence of blocked elements is assessed under two imaging scenarios. For the transcostal simulation, the rib is oriented along the lateral dimension of the transducer and the B-mode images are reconstructed for the receive aperture growing in the perpendicular (i.e., elevation) direction. This ensures that the lateral resolution is the same between the (growing aperture) images, which makes it possible to assess the potential loss of image quality due to noise on the blocked elements only. In the *in vivo* transcostal acquisitions, the orientation of the rib with respect to the array surface was difficult to control, and for a diagonal orientation, both noise level and the lateral resolution of the B-mode slices are affected during the receive aperture growth.

Examples of growing-aperture B-mode images of liver reconstructed from the control and transcostal simulations are shown in Figs. 5 and 6, respectively. The receive apertures are increased along the elevation dimension of the array and the images are shown at 33% and 100% of the total physical aperture. Under each B-mode image from the transcostal simulation, the image of element amplitude from Fig. 3(a) is recreated and the locations of enabled receive elements are shaded in red. As the schematics show, the receive aperture grows to include the blocked elements first, and the nonblocked elements are gradually added afterward at larger aperture sizes. All images are log-compressed and displayed using a 60-dB dynamic range, except for the 33%-Rx-aperture image created from the transcostal simulation, which is displayed using an extended dynamic range (80 dB) to show attenuated signals at larger depths. In the 33%-Rx-aperture transcostal image, the region inside the lesion used to compute contrast and CNR is demarcated with white dashed lines.

The lesion is visible in all images displayed for the control simulation (Fig. 5). As the receive aperture grows in elevation, the slice thickness decreases and clutter inside the lesion is reduced. In the images created from the transcostal simulation (Fig. 6), the near-field region is brighter and the signals at larger depths are more attenuated than in the matching control scans. Furthermore, in the 33%-Rx-aperture transcostal image, which is beamformed almost exclusively using the signals from the blocked elements, the anechoic lesion at 6-cm depth cannot be observed. The lesion visibility improves as the signals from the nonblocked elements are included in the image.

Contrast and CNR of the anechoic lesions observed in Figs. 5 and 6 are plotted as functions of the receive-aperture size in Fig. 7. For the control simulation, both contrast and CNR increase gradually as the receive aperture grows reaching maxima of 15.9 dB and 1.58, respectively, at full aperture. For the transcostal simulation, the image quality metrics remain low as the images are beamformed using only blocked elements. Specifically, as the receive aperture grows to include 33% of the total array size, contrast and CNR for the transcostal simulation increase from 2.14 to 3.1 dB, and from 0.34 to 0.49, respectively. Following the same change in the receive aperture for the control simulations, lesion contrast and CNR

Author Manuscript Author Manuscript Author Manuscript Author Manuscript

increase from 9.36 to 14 dB, and from 1.19 to 1.49, respectively. Lesion contrast and CNR (computed for the transcostal simulation) start to improve as the nonblocked elements are added to the aperture, reaching maxima of 14.8 dB and 1.42 at full receive aperture. These results indicate that the blocked-element signals are dominated by noise and do not significantly contribute to lesion visibility.

Sample B-mode images of *in vivo* liver vasculature reconstructed using receive apertures of different sizes are shown in Figs. 8 and 9. The images are created from the same pair of abdominal and transcostal acquisitions used to generate Figs. 3 and 4. To assess the effectiveness of basic blocked-element compensation, the images in each figure are beamformed using the upper 8%, 67%, and 100% of receive array elements, which for the transcostal acquisition implies that the smallest receive aperture contains the nonblocked elements only, and the blocked elements are added gradually at larger aperture sizes. The locations of receive elements used to create the transcostal B-mode scans are denoted in a similar manner as in Fig. 6, using the maps from Fig. 3(b). The angled orientation of the ribs for this acquisition means that the effective 2-D aperture cannot be described as two separate functions. The presented results for the aperture growth in elevation dimension are relevant to 1-D arrays with partially blocked elements, which are more common. The results for the aperture growth in the lateral dimension are similar and are omitted. All images are displayed on a decibel scale with the dynamic range chosen to optimally visualize the vasculature of interest for a given acquisition.

Fig. 8 shows selected images of different Rx-aperture sizes created from the abdominal acquisition. A blood vessel located at 7-cm depth at the center of the FOV is apparent for all three receive-aperture sizes. The image beamformed with only 8% of available receive elements is saturated with noise and the shape of the vessel cross section is not clearly conveyed. The image reconstructed using 67% of available receive elements shows significantly reduced noise and improved definition of vessel boundaries compared to its 8%-aperture counterpart. The image beamformed using all receive elements indicates even further reduction of clutter inside of the vessel lumen.

Fig. 9 shows the *in vivo* images created from the transcostal acquisition, using the receive apertures of the same sizes as those used to create the images in Fig. 8. The image reconstructed using only the upper 8% of receive elements is overwhelmed with clutter and no hypoechoic structures can be identified. A large blood vessel can be observed at about 11-cm depth at the right-hand side of FOV in the images reconstructed using 67% and 100% of the available receive aperture. The 67%-receive-aperture image is reconstructed with most of the blocked elements turned OFF and it displays clearer vessel lumen and more pronounced vessel walls compared with its full-Rx-aperture counterpart.

Contrast and CNR of the vessels observed in Figs. 8 and 9 are plotted over a range of receive-aperture sizes in Fig. 10. The image quality metrics obtained for each acquisition are plotted on separate graphs. Contrast and CNR values that correspond to the images in Figs. 8 and 9 are denoted with circles, while the vertical dashed lines are used to indicate the aperture size at the maximum contrast/CNR for the transcostal acquisition.

Author Manuscript Author Manuscript Author Manuscript Author Manuscript

For the abdominal acquisition (Fig. 10), both contrast and CNR of the vessel increase as more elements are used to beamform the images, reaching maxima of 11.4 dB and 1.57, respectively, at full aperture. For the transcostal acquisition (Fig. 10), the image-quality metrics improve as the receive aperture grows (in elevation) until noisy signals from the blocked elements are introduced. The maximum values of contrast and CNR are 10 dB and 1.46, respectively, and are both measured when (the upper) 66.7% of the available receive aperture is used to beamform an image. When the blocked elements are turned ON and included in image reconstruction, contrast and CNR decrease to 9 dB and 1.36, respectively.

Table III summarizes changes in contrast and CNR following the receive-aperture growth for the abdominal and transcostal acquisitions in all five subjects. Changes in image quality metrics are recorded over the region of blocked elements for the transcostal acquisitions, and over the same receive aperture sizes for the matching abdominal acquisitions. Similar trends are observed across the subjects. Adding signals from the blocked elements results in the mean drop in contrast of 19.2%, while the average drop in CNR (computed over the same changes in the receive apertures) is measured at 10%. Therefore, excluding signals from the blocked elements in the image has the potential to partially recover losses in contrast and CNR.

IV. Discussion

A. Detection of Blocked Elements

The simulation and *in vivo* results demonstrate that blocked elements can be detected based on low amplitude and cross-correlation values of their echoes. In this paper, the elements were declared as blocked if their average amplitude was −8 dB or lower (relative to the maximum element amplitude in the aperture), and if their average nearest-neighbor cross correlation was less than 0.5. For the simulated transcostal scan, blocked elements are detected in the top four rows of the 2-D aperture, as seen in the channel-amplitude and cross-correlation images in Fig. 2(b). The speed-of-sound maps in Fig. 1 show that this part of the aperture is located directly above the rib and is expected to be in its acoustic shadow. The validity of the blocked-element-detection method is further supported with the matching control simulation, where bone was assigned the acoustic properties of the surrounding connective tissue [Fig. 1(b)]. The resulting images of element amplitude and the nearest-neighbor cross correlation are uniform and display high values across the elements [Fig. 2(a)], which confirms the absence of acoustic obstacles and means that the blocked elements detected in the matching transcostal simulations are due to ribs only.

The images reconstructed from the *in vivo* acquisitions are consistent with the simulation results, and suggest that matrix arrays can improve detection of blocked elements compared to 1-D arrays. In the images of average element amplitude and average nearest-neighbor cross correlation reconstructed from a transcostal liver scan [Fig. 3(b)], a region of low values can be observed in the bottom-right corner, and is attributed to a rib blocking that part of the aperture. The shape of the blocked region suggests that sampling apertures along only one dimension would lead to blurring of the transition band (between blocked and nonblocked regions) making detection by thresholding more difficult. The images created

Author Manuscript Author Manuscript Author Manuscript Author Manuscript

from the matching abdominal acquisition [Fig. 3(a)] display uniformity across the elements in the absence of an acoustic obstacle.

It is worth noting that the blocked elements were successfully detected using signals from speckle targets and in the presence of acoustic noise. The element signals from the simulated and *in vivo* transcostal acquisitions are corrupted by clutter as indicated in the corresponding B-mode images (Figs. 6 and 9). Nevertheless, the element amplitude and the nearest-neighbor cross correlation in Figs. 2(b) and 3(b) show reduced noise after depth averaging (4 cm around the Tx focus). This allows for a clear distinction between the blocked and nonblocked parts of the apertures.

B. Basic Blocked-Element Compensation on Anechoic and Hypoechoic Targets

Signals received on the blocked elements are dominated by noise, which degrades the visibility of anechoic/hypoechoic targets. For example, in the B-mode image that is created from the transcostal simulations and using the upper 33% of the receive aperture, the anechoic lesion at 6-cm depth is not visible (Fig. 6). As observed in the corresponding channel-amplitude and cross-correlation images [Fig. 2(b)], the receive aperture used to create this B-mode is comprised almost entirely of the blocked elements. On the other hand, the B-mode image created from the matching control simulations and using the same-size Rx aperture shows the lesion with a contrast of 9.36 dB and CNR of 1.19 (Figs. 6 and 7).

The B-mode images reconstructed from the *in vivo* acquisitions indicate that turning OFF blocked elements could improve visualization of the anechoic and hypoechoic targets. As observed in the B-mode images created from the transcostal acquisition in Fig. 9, when the blocked elements are added to the Rx aperture to increase its size from 66% to 100% (of the total array size), vessel contrast and CNR decrease from 10 to 9 dB, and from 1.46 to 1.36, respectively. In the matching abdominal acquisition, the vessel contrast and CNR increase monotonically with the receive aperture size (Fig. 8). Similar trends in vessel contrast/CNR were observed in the other four subjects for their respective transcostal and abdominal acquisitions (Table III). The loss of image quality associated with the *in vivo* transcostal acquisitions can be attributed to noise on the blocked elements and to decrease in the effective aperture size caused by diagonal orientation of the rib. In particular, comparing the right-hand plots in Fig. 10 to the amplitude and cross-correlation images in Fig. 3(b) suggests that when a majority of elements in a row are blocked, adding that row to the aperture will likely degrade image quality. When extended to 1-D arrays, this result implies that partially blocked elements with less than 50% of effective area should not be included in image reconstruction.

The aforementioned conclusions of the *in vivo* study are not affected by variations of contrast and CNR measurements across the patients. In particular, the large standard deviations in Table III can be attributed to the fact that the level of acoustic noise and overall image quality (both of which affect target visibility) is patient-dependent. In addition, for the transcostal acquisitions, the size and location of the blocked regions change with the Tx beam direction (as shown in the channel amplitude and cross-correlation images in Fig. 4); this kind of variation makes it more difficult to track incremental changes in vessel contrast and CNR in the presence of blocked elements. Nevertheless, the presented *in vivo* results

Author Manuscript Author Manuscript Author Manuscript Author Manuscript

show a clear difference in trends in contrast/CNR between the transcostal and abdominal acquisitions. For both image quality metrics, the difference of the means of the two groups (i.e., abdominal and transcostal acquisitions) is larger than the sum of their respective standard deviations (Table III).

Simulation results support the conclusions drawn from the *in vivo* B-mode images despite the differences between the contrast/CNR curves for the control simulation (Fig. 7) and their counterparts for the *in vivo* abdominal acquisition [Fig. 10(a)]. Specifically, the B-mode images created from the control simulation do not show significant improvements in lesion visibility for larger receive apertures. This trend may be explained by imperfections in the tissue model employed in simulation. For example, all tissue structures used in the model are detected from photographs of tissue that have limited resolution [14], which in turn makes it difficult to determine reverberation caused by small inhomogeneities (in the subcutaneous tissue layer). If the reverberation is too strong, it can lead to a loss of signal coherence across the receive aperture and reduce improvements in target visibility with increasing aperture size. To circumvent the issue, the simulated control images created from the smaller Rx-apertures (across which coherence is preserved) were compared to their transcostal counterparts that contained signals from the blocked elements only. In that case, the lesion contrast and CNR exhibit growth for the control case, and they remain low for the simulated transcostal scan contributing to the claim that the blocked elements carry noise and can degrade lesion visibility.

V. Conclusion

We have demonstrated a method to detect the array elements that are blocked by ribs based on the amplitude and cross correlation of their signals. The element signals collected from speckle targets and in the presence of clutter during a simulated and *in vivo* transcostal scans show that the average element amplitude and the average nearest-neighbor cross correlation are lower for the blocked elements than for than the remainder of the 2-D aperture. The growing aperture B-mode images created from these data indicate that the blocked elements are dominated by noise and that turning them OFF has a potential to improve visibility of liver vasculature. Such basic blocked-element compensation in combination with the amplitude-based blocked-element detection could be integrated in the work flow of a commercial ultrasound system and performed in real time. In the companion paper, the blocked-element detection algorithm is extended to large synthetic apertures, and is a prerequisite for adaptive compensation schemes that aim at improving the focus quality and reducing the near-field reverberation clutter.

Acknowledgments

This work was supported by the National Institute of Biomedical Imaging and Bioengineering under Grant R37-HL096023 and Grant R01-EB017711.

The authors would like to thank the Ultrasound Division, Siemens Medical Solutions USA, Inc., for their in-kind and technical support. They would also like to thank Dr. M. Palmeri, Dr. B. Byram, and L. Kuo for their help with the *in vivo* data acquisitions.

Author Manuscript Author Manuscript Author Manuscript Author Manuscript

References

1. Hinkelman LM, Szabo TL, Waag RC. Measurements of ultrasonic pulse distortion produced by human chest wall. J Acoust Soc Amer. 1997; 101(4):2365–2373. [PubMed: 9104034]
2. Herth FJF, Becker HD. Transthoracic ultrasound. Respiration. 2003; 70(1):87–94. [PubMed: 12584397]
3. Wernecke K, Vassallo P, Pötter R, Lückener HG, Peters PE. Mediastinal tumors: Sensitivity of detection with sonography compared with ct and radiography. Radiology. 1990; 175(1):137–143. [PubMed: 2179987]
4. Li PC, Flax SW, Ebbini ES, O'Donnell M. Blocked element compensation in phased array imaging. IEEE Trans Ultrason, Ferroelect, Freq Control. Jul; 1993 40(4):283–292.
5. Lu XM. Comprehensive design considerations for 2D matrix arays. Proc IEEE Ultrason Symp. Nov. 2008 :1134–1137.
6. O'Donnell M, Engeler WE. Correlation-based aberration correction in the presence of inoperable elements. IEEE Trans Ultrason, Ferroelect, Freq Control. Nov; 1992 39(6):700–707.
7. Huang S-W, et al. Detection and display of acoustic window for guiding and training cardiac ultrasound users. Proc SPIE. Mar.2014 9040:904014.
8. Lovstakken L, Orderud F, Torp H. P2b-14 real-time indication of acoustic window for phased-array transducers in ultrasound imaging. Proc IEEE Ultrason Symp. Oct.2007 :1549–1552.
9. Ballard JR, Casper AJ, Wan Y, Ebbini ES. Adaptive transthoracic refocusing of dual-mode ultrasound arrays. IEEE Trans Biomed Eng. Jan; 2010 57(1):93–102. [PubMed: 19651547]
10. Aubry JF, Pernot M, Marquet F, Tanter M, Fink M. Transcostal high-intensity-focused ultrasound: *Ex vivo* adaptive focusing feasibility study. Phys Med Biol. 2008; 53(11):2937–2951. [PubMed: 18475006]
11. Khokhlova VA, Bobkova SM, Gavrilov LR. Focus splitting associated with propagation of focused ultrasound through the rib cage. Phys Acoust. 2010; 56(5):622–632.
12. Gélat P, Haar GT, Saffari N. Modelling of the acoustic field of a multi-element hifu array scattered by human ribs. Phys Med Biol. 2011; 56(17):5553. [PubMed: 21828903]
13. Pinton GF, Dahl J, Rosenzweig S, Trahey GE. A heterogeneous nonlinear attenuating full-wave model of ultrasound. IEEE Trans Ultrason, Ferroelect, Freq Control. Mar; 2009 56(3):474–488.
14. Pinton GF. Three dimensional full-wave nonlinear acoustic simulations of ultrasound imaging and therapy in the entire human body. Proc IEEE Ultrason Symp. Oct.2012 :142–145.
15. Goss SA, Johnston RL, Dunn F. Compilation of empirical ultrasonic properties of mammalian tissues. J Acoust Soc Amer. 1978; 64(2):423–457. [PubMed: 361793]
16. Goss SA, Johnston RL, Dunn F. Compilation of empirical ultrasonic properties of mammalian tissues. II. J Acoust Soc Amer. 1980; 68(1):93–108. [PubMed: 11683186]
17. Jakovljevic M, Byram B, Hyun D, Dahl JJ, Trahey GE. Short-lag spatial coherence imaging on matrix arrays, Part II: Phantom and *in vivo* experiments. IEEE Trans Ultrason, Ferroelect, Freq Control. Jul; 2014 61(7):1113–1122.
18. Bottenus N, Byram B, Trahey G. A synthetic aperture study of aperture size in the presence of noise and *in vivo* clutter. Proc SPIE. Mar.2013 8675:86750S.
19. Mallart R, Fink M. Adaptive focusing in scattering media through sound-speed inhomogeneities: The van Cittert Zernike approach and focusing criterion. J Acoust Soc Amer. 1994; 96(6):3721–3732.

Author Manuscript Author Manuscript Author Manuscript Author Manuscript

Biographies

Marko Jakovljevic received the B.S. degree from The University of Texas at Austin, Austin, TX, USA, in 2009, and the Ph.D. degree from Duke University, Durham, NC, USA, in 2015, under the supervision of Dr. Trahey.

He is currently a Post-Doctoral Fellow with the Department of Radiology, School of Medicine, Stan-ford University, Stanford, CA, USA. His current research interests include coherence imaging, synthetic aperture beamforming, and signal processing in general.

Gianmarco F. Pinton was born in Milan, Italy, in 1979. He received the B.S. degree in physics and the B.S.E. degree in biomedical engineering, and the M.S. in mathematics and the Ph.D. degree in biomedical engineering from Duke University, Durham, NC, USA, in 2001 and 2007, respectively.

He is currently an Assistant Professor with the Joint Department of Biomedical Engineering, University of North Carolina at Chapel Hill and North Carolina State University, Chapel Hill, NC, USA. His research interests include nonlinear acoustic and shear wave propagation and brain imaging.

Jeremy J. Dahl (M’11) was born in Ontonagon, MI, USA, in 1976. He received the B.S. degree in electrical engineering from the University of Cincinnati, Cincinnati, OH, USA, in 1999, and the Ph.D. degree in biomedical engineering from Duke University, Durham, NC, USA, in 2004.

Author Manuscript Author Manuscript Author Manuscript Author Manuscript

He is currently an Assistant Professor with the Department of Radiology, School of Medicine, Stan-ford University, Stanford, CA, USA. His current research interests include adaptive beamforming, noise in ultrasonic imaging, and radiation force imaging methods.

Gregg E. Trahey (S'83–M'85) received the B.G.S. and M.S. degrees from the University of Michigan, Ann Arbor, MI, USA, in 1975 and 1979, respectively, and the Ph.D. degree in biomedical engineering from Duke University, Durham, NC, USA, in 1985.

He served in the Peace Corps, Washington, DC, USA, from 1975 to 1978. He was a Project Engineer with the Emergency Care Research Institute, Plymouth Meeting, PA, USA, from 1980 to 1982. He is currently a Professor with the Department of Biomedical Engineering, Duke University, and holds a secondary appointment with the Department of Radiology, Duke University Medical Center, Durham. He is conducting research in adaptive phase correction, radiation force imaging methods, and 2-D flow imaging in medical ultrasound.

Author Manuscript Author Manuscript Author Manuscript Author Manuscript

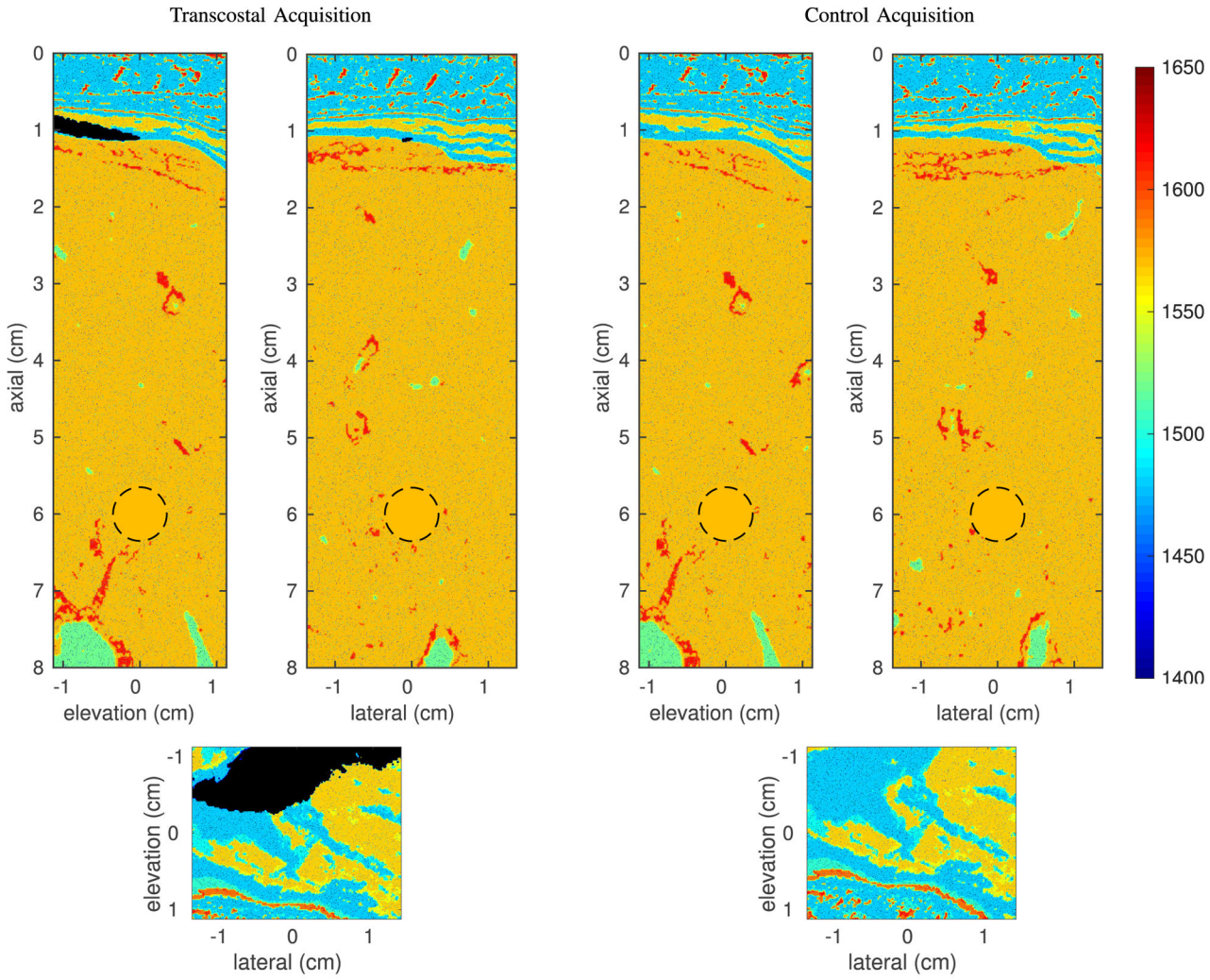

Fig. 1.

Orthogonal slices of the speed of sound maps used for the transcostal simulations (left) and for the control simulations (right). The elevation and lateral slices are taken through the center of the volumes, while the C-scan is taken at 1-cm depth. For the transcostal case, a rib can be observed at about 1-cm depth in the elevation slice and in the C-scan; it is colored in black and its speed of sound is 800 m/s. The rest of the tissue is displayed over the dynamic range shown in colorbar. In the acoustic maps used for the control simulations, ribs are replaced by the connective tissue. In the lateral and elevation slices, the lesion boundaries are denoted using a black dashed line.

Author Manuscript Author Manuscript Author Manuscript Author Manuscript

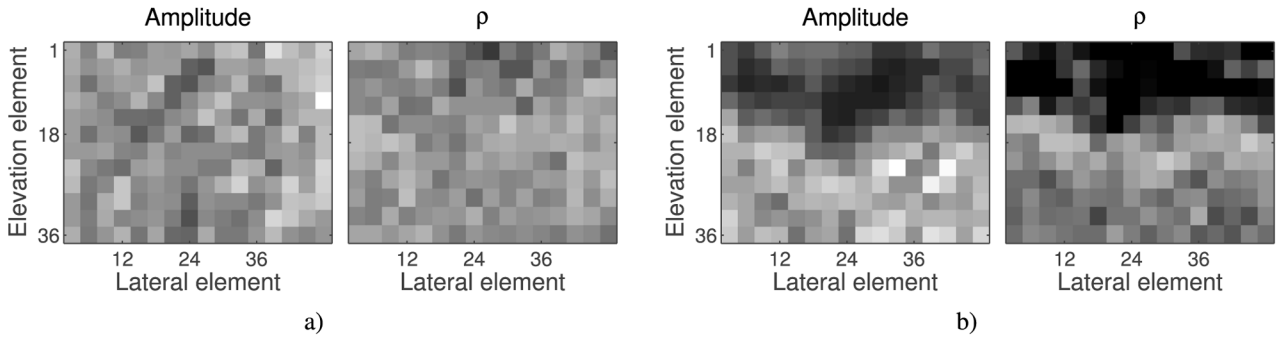

Fig. 2.

Average amplitude (left) and average nearest-neighbor normalized cross correlation (right) of the simulated element-signals collected from the 2-D array (a) during simulated control and (b) transcostal liver scans. Averaging is done in the axial dimension between 4- and 8-cm depth. For the control simulation, in which bone was substituted with connective tissue properties, both amplitude and nearest-neighbor cross correlation of the element signals are uniform across the array. For the transcostal simulation, the top four rows of elements show lower amplitude and cross correlation values than the rest of the aperture, corresponding to elements blocked by a rib (Fig. 1).

Author Manuscript Author Manuscript Author Manuscript Author Manuscript

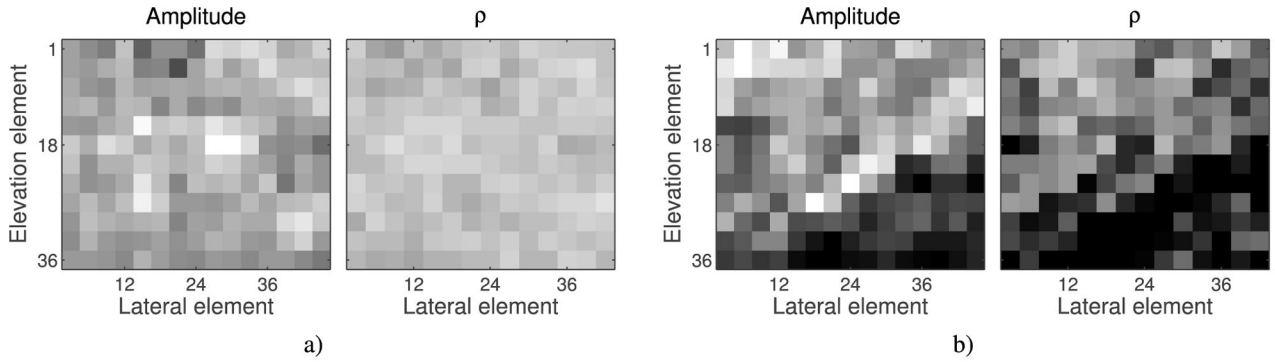

Fig. 3.

Average element amplitude (left) and average nearest-neighbor normalized cross correlation (right) displayed across the 2-D apertures for (a) *in vivo* liver scan through the abdomen and (b) matching liver scan through the ribs. The images are formatted in a similar way as in Fig. 2. For the abdominal acquisition, both quantities appear relatively uniform throughout the extent of the aperture indicating echoes have been received without significant obstruction. For the transcostal acquisition, a region of low values in the bottom-right corner (of both images) is attributed to a rib blocking that part of the aperture. The shape of the blocked region suggests diagonal orientation of the rib with respect to the array surface.

Author Manuscript Author Manuscript Author Manuscript Author Manuscript

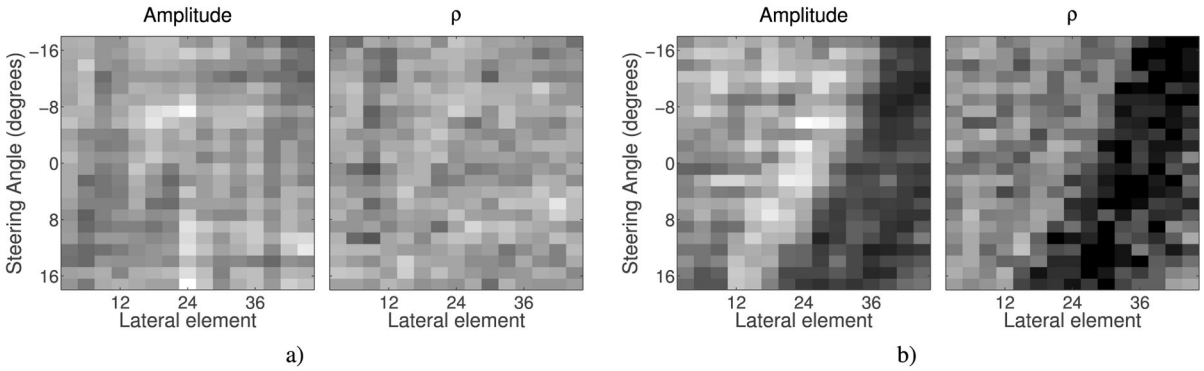

Fig. 4.

Average element amplitude (left) and average nearest-neighbor cross correlation (right) displayed as functions of the transmit beam direction for a single row of elements, and for (a) same abdominal and (b) transcostal acquisitions used to create the images in Fig. 3. For the abdominal acquisition, high values across both images indicate that no acoustic obstacles are encountered as the transmit beam is swept in the lateral plane. For the transcostal acquisition, the shape of the region of low values in both amplitude and cross correlation images indicates that the number of blocked elements (in the row of interest) decreases as the transmit beam is steered away from the rib.

Author Manuscript Author Manuscript Author Manuscript Author Manuscript

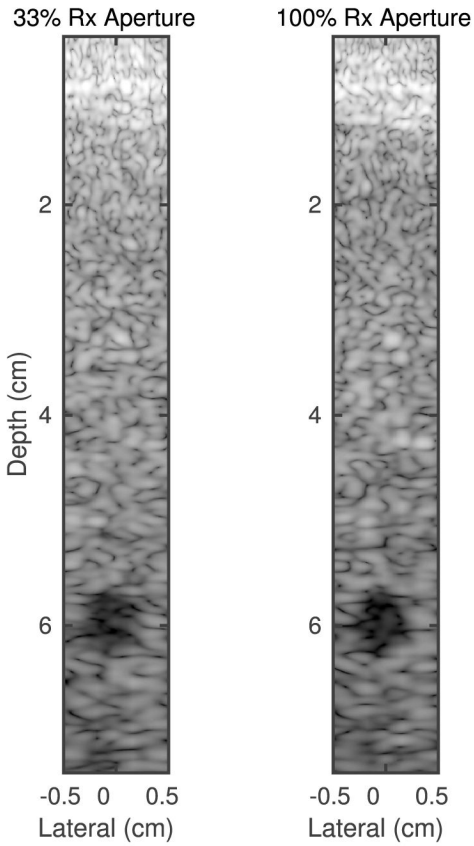

Fig. 5.

B-mode images of liver created from the simulated control acquisition, where ribs were assigned acoustic properties of the surrounding connective tissue. The images are reconstructed using the receive apertures that contain the upper 33% of elements (left) and all of the array elements (right). An anechoic lesion inserted in the liver model can be observed at 6-cm depth in both images. Increasing the extent of receive aperture in elevation dimension reduces slice thickness, which results in lower clutter inside the lesion and improves the definition of its edges. The images are log compressed and displayed using the 60-dB dynamic range.

Author Manuscript Author Manuscript Author Manuscript Author Manuscript

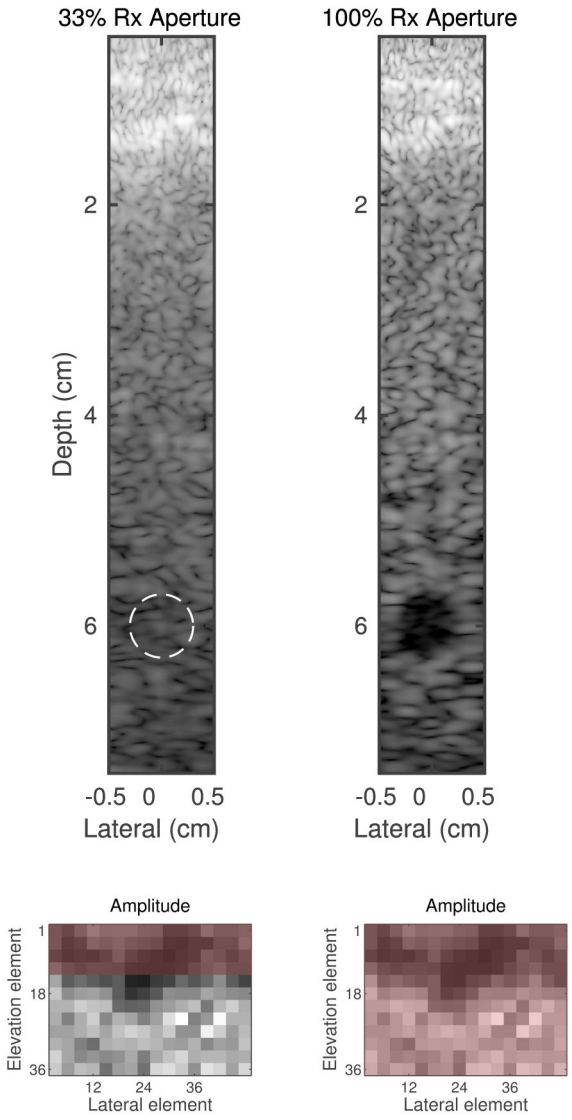

Fig. 6.

B-mode images of liver reconstructed from the simulated transcostal acquisition where a part of the aperture is blocked by a rib. Under each B-mode image is the image of average element amplitude, with the locations of used receive elements shaded in red. The 33%-Rx-aperture B-mode image (left), which is reconstructed using mainly blocked elements, is dominated by noise and no structures can be identified. The lesion visibility is improved in the full-Rx-aperture B-mode image (right) as it contains more signals from the nonblocked elements. A white dashed circle in the 33%-Rx-aperture B-mode image denotes the extent of the lesion in the liver model.

Author Manuscript Author Manuscript Author Manuscript Author Manuscript

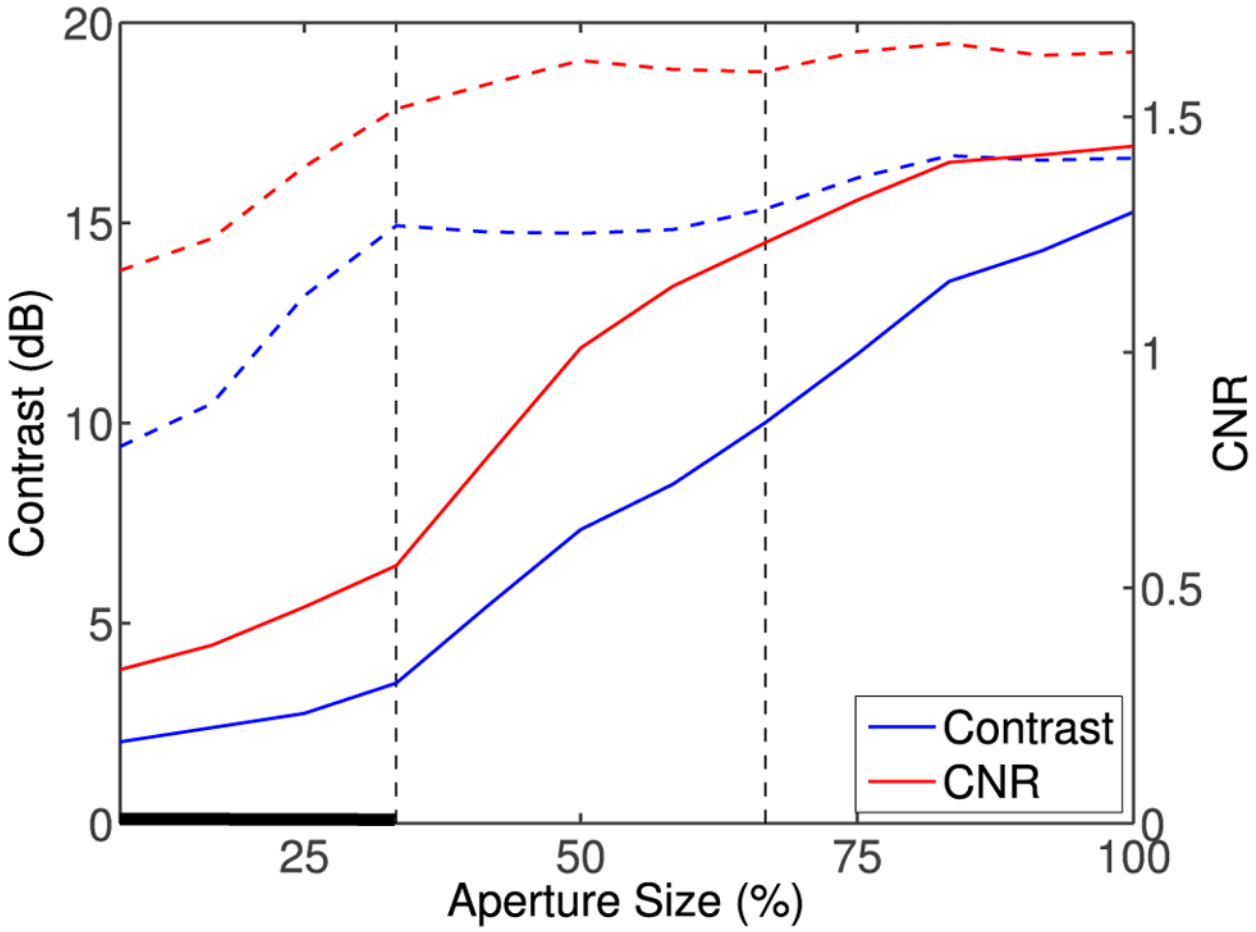

Fig. 7.

Contrast and CNR of the anechoic lesion in the liver model measured as functions of the receive-aperture size for the simulated control scan (dashed lines) and the simulated transcostal scan (solid lines). The two image quality metrics are presented on the same graph using the dual-axis plots with contrast values displayed on the left *y*-axis and CNR values displayed on the right *y*-axis. For the control simulation, both contrast and CNR increase gradually with the receive aperture size. For the transcostal simulation, the image-quality metrics remain low initially, as the Rx aperture contains mainly blocked elements, and then they grow as the signals from the nonblocked elements are added to the image. As a reference, the black vertical dashed lines denote sizes of the Rx-apertures used to reconstruct the B-mode images in Figs. 5 and 6. The blocked part of the aperture (during the transcostal simulation) is denoted with a thick black line along the *x*-axis.

Author Manuscript Author Manuscript Author Manuscript Author Manuscript

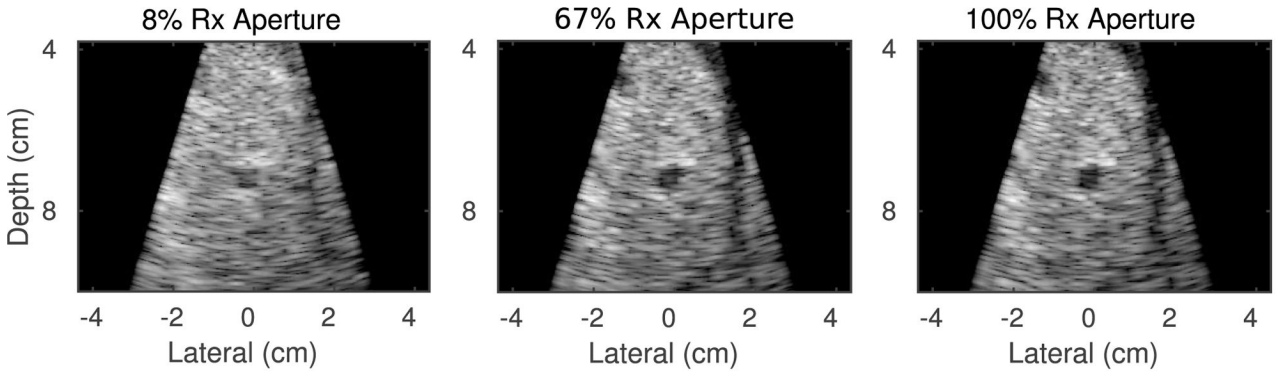

Fig. 8.

B-mode images of *in vivo* liver vasculature acquired through the abdomen and reconstructed using receive apertures of different sizes. Left to right: images are reconstructed using the receive apertures that increase in elevation dimension and contain the upper 8%, 67%, and 100% of array elements. All images are log compressed and displayed using a 45-dB dynamic range. A vessel located in the center of FOV at 7-cm depth can be observed for all three receive-aperture sizes. Increasing the receive aperture reduces clutter and improves visibility of the vessel in the resulting images.

Author Manuscript Author Manuscript Author Manuscript Author Manuscript

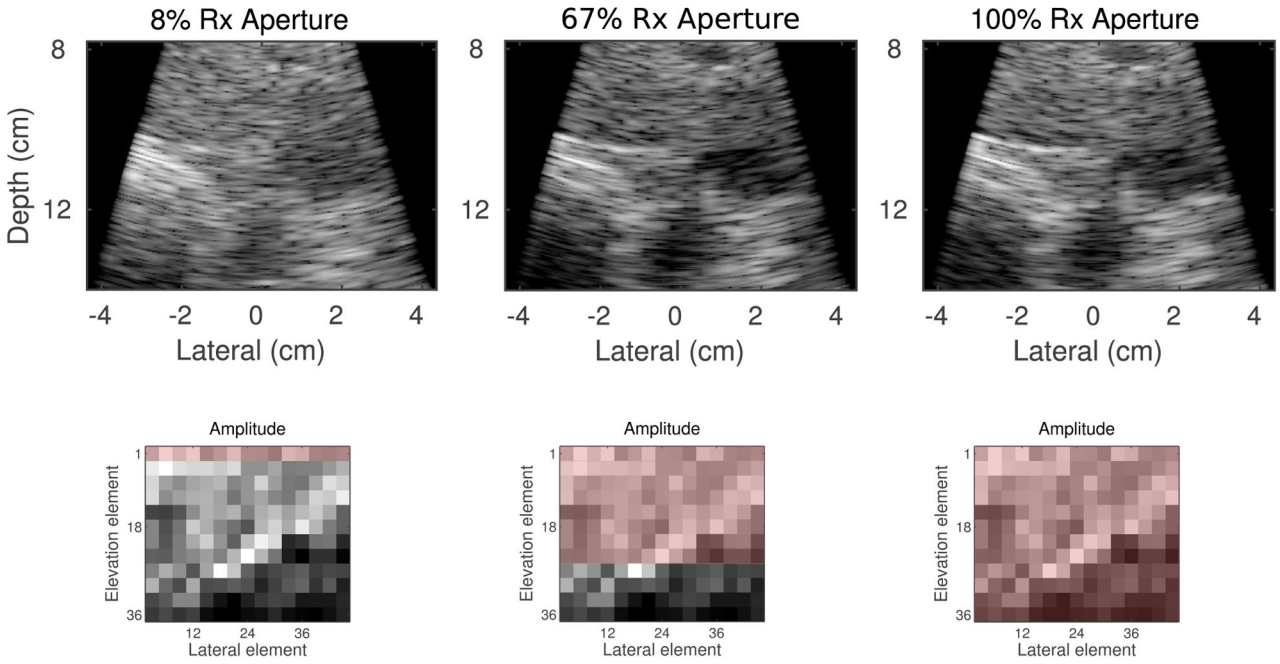

Fig. 9.

B-mode images of *in vivo* liver vasculature acquired transcostally and reconstructed using the receive apertures of the same sizes as in Fig. 8. The receive aperture is grown to gradually transition from nonblocked to blocked region of the array, and is denoted with red overlay in the element-amplitude images from Fig. 3(b) under each B-mode. All B-mode images are log compressed and displayed using a 45-dB dynamic range. When only 8% of receive elements are used, the B-mode scan is overwhelmed with noise and no structures can be identified. When 67% of the receive aperture is used and most of the blocked elements are still turned OFF, a large blood vessel can be observed in the right-hand side of FOV at about 9-cm depth. The B-mode image created using the full receive aperture (i.e., the uncompensated image) includes the noise from the blocked elements and displays higher levels of clutter inside the vessel compared to its 67%-receive-aperture counterpart.

Author Manuscript Author Manuscript Author Manuscript Author Manuscript

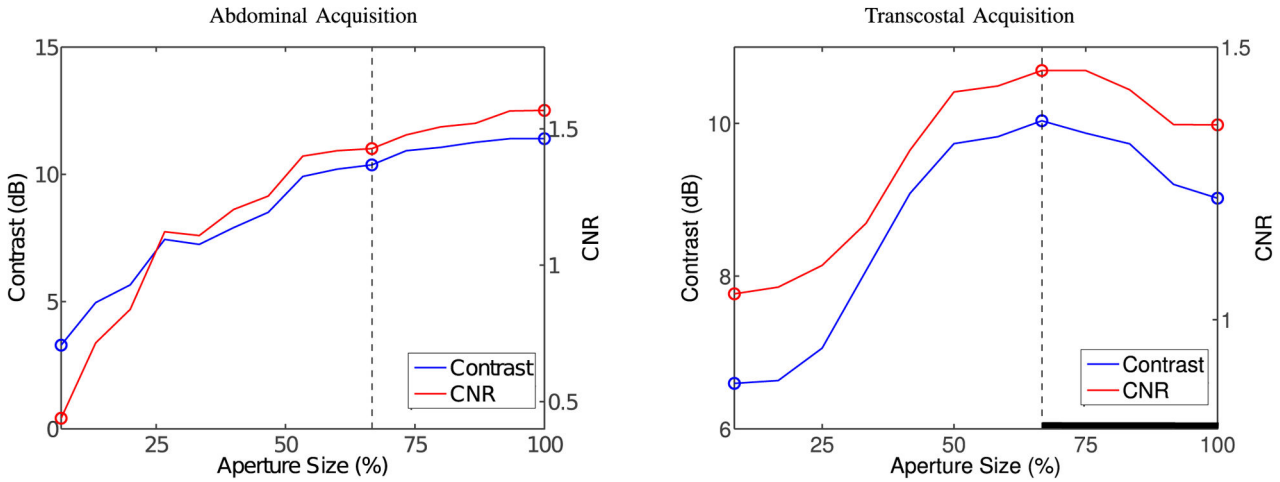

Fig. 10.

Contrast and CNR as functions of receive-aperture size for the blood vessels captured during the abdominal acquisition (left) and transcostal acquisition (right). Colored circles denote the contrast and CNR values that correspond with the images in Figs. 8 and 9. For the abdominal acquisition (left), both contrast and CNR increase with receive aperture size reaching maxima of 11.4 dB and 1.57, respectively, at full aperture. For the transcostal acquisition (right), the two image-quality metrics improve as the receive aperture grows until signals from the blocked elements are included in the image. The image is optimally compensated when the vessel contrast and CNR reach maxima, at the 66.7% receive aperture. This aperture size is denoted by a black vertical dashed line in both plots. A black thick line along the *x*-axis is used to denote blocked part of the aperture during the transcostal acquisition.

Author Manuscript

Author Manuscript

Author Manuscript

Author Manuscript

TABLE I

Acoustic Properties of Different Tissue Types Used in Simulation

Tissue	B/A	α (dB/MHz per cm)	c_0 (m/s)	ρ_0 (kg/cm^3)
Homogeneous	9.0	0.50	1540	1000
Fat	9.6	0.40	1479	937
Muscle	8.0	0.15	1550	1070
Connective	8.0	0.68	1613	1120
Liver	7.6	0.50	1570	1064
Bone	0	5	800	550

Author Manuscript

Author Manuscript

Author Manuscript

Author Manuscript

TABLE II

Simulated Transducer Properties

Number of Elements in Lateral	48
Number of Elements in Elevation	36
Center Frequency	2.5 MHz
Bandwidth	50%
Lateral Pitch	0.4 mm
Elevation Pitch	0.4 mm
Transmit Focus	4 cm

Author Manuscript Author Manuscript Author Manuscript Author Manuscript

TABLE III

Changes in Image Quality Following the Receive Aperture Growth for Transcostal and Abdominal Acquisitions in Five Different Patients

Patient number	Change in Contrast (%)		Change in CNR (%)		Aperture increase (% of Rx aperture)
	Transcostal	Abdominal	Transcostal	Abdominal	
1	−32.9	17.7	−21.9	20.0	56.2
2	−17.4	31.1	−3.4	−2.9	50.0
3	−15.9	36.8	−6.8	27.6	50.0
4	−18.2	125.3[a]	−12.5	103.8[a]	66.7
5	−11.7	57.4	−5.9	37.7	50.0
means	−19.2	35.7	−10.1	20.6	54.6
std	8.0	16.5	7.4	17.3	7.3

[a]Lack of a good acoustic window through the abdomen resulted in low image quality and extremely large changes in contrast and CNR for this acquisition. These values have been treated as outliers and have not been included in mean/standard deviation calculations.

IEEE Trans Ultrason Ferroelectr Freq Control. Author manuscript; available in PMC 2018 February 28.